From Geometry to Activity: A Quantitative Analysis of WO₃/Si Micropillar Arrays for Photoelectrochemical Water Splitting

Yihui Zhao, Pieter Westerik, Rudi Santbergen, Erwin Zoethout, Han Gardeniers, Anja Bieberle-Hütter*

Dr. Y. Zhao, Dr. E. Zoethout, Dr. A. Bieberle-Hütter
Dutch Institute for Fundamental Energy Research (DIFFER),
5600 HH Eindhoven, The Netherlands
E-mail: A.Bieberle@differ.nl

Dr. P. Westerik, Prof. Dr. H. Gardeniers
Mesoscale Chemical Systems,
MESA+ Institute for Nanotechnology, University of Twente,
7500 AE Enschede, The Netherlands

Dr. R. Santbergen
Photovoltaic Materials and Devices group, Delft University of Technology,
2600 AA Delft, The Netherlands

Abstract: The photoelectrochemical (PEC) activity of microstructured electrodes is still low despite the highly enlarged surface area and enhanced light harvesting. To obtain a deeper understanding of the effect of 3D geometry on the PEC performance, well-defined WO₃/n-Si and WO₃/pn-Si micropillar arrays are fabricated and subjected to a quantitative analysis of the relation between the geometry of the micropillars (length, pitch) and their PEC activity. For WO₃/n-Si micropillars, it is found that the photocurrent increases for WO₃/n-Si pillars, but not in proportion to the increase of surface area that results from increased pillar length or reduced pillar pitch. Optical simulations show that a reduced pillar pitch results in areas of low light intensity due to shadowing effect. For WO₃/pn-Si micropillar photoelectrodes, the p-n junction enhances the photocurrent density up to a factor of 4 at low applied bias potential (0.8 V vs RHE) compared to the WO₃/n-Si. However, the enhancement in photocurrent density increases

first and then decreases with reduced pillar pitch, which scales with the photovoltage generated

by the p-n junction. This is related to an increased dead layer of the p-n junction Si surface,

which results in a decreased photovoltage even though the total surface area increases.

1. Introduction

Hydrogen production from photoelectrochemical (PEC) water splitting using

semiconductor photoelectrodes is a promising pathway towards the utilization of renewable

energy for solar fuel applications[1–3]. For PEC water splitting, the oxygen evolution reaction

(OER), which occurs at the photoanode, is more complex because it requires multiple bond

rearrangements that involve the removal of four electrons and two protons from two H_2O

molecules.[2,4,5] In recent years, metal oxide films, such as TiO_2, WO_3, Fe_2O_3, and $BiVO_4$, have

been studied as the photoanode for catalysing PEC water oxidation reactions due to their

suitable band gap, chemical stability and low cost[6–14]. However, the narrow spectral light

absorption band and poor charge transport properties of these materials are certainly key factors

in limiting the PEC efficiency[15–17]. Compared to these metal oxides, silicon (Si) has

controllable electrical conductivity and a smaller band gap (1.1 eV), which can address the

deficiencies of metal oxides functional films[18,19]. Nevertheless, Si has poor chemical stability

because it is rapidly oxidized in aqueous solution under solar illumination or under anodic

bias[20]. In this sense, metal oxide films combined with Si substrates show a complementary

relation and offer a promising model for PEC electrode design.

Furthermore, nano-/microstructured Si could concurrently reduce light reflection by

trapping light inside the structures and provide more catalytic sites by increasing surface area.

Based on this, research has been focused on nano-/microstructured Si coated with metal oxide

films for PEC water splitting electrodes[18,21,22]. TiO_2 coated Si nanowires showed 2.5 times

higher photocurrent density on the projected area than the corresponding planar TiO_2/Si[6] at

1.23 V vs RHE. Fe_2O_3 on Si nanowires exhibited a current density of about 0.9 mA/cm^2 at

1.23 V vs RHE, which was 2.5 times higher on the projected area than that of planar Fe_2O_3/FTO (FTO, fluorine doped tin oxide)[23]. Based on micropillar arrays, a porous structure of WO_3 was built on the surface of Si micropillars. This increased the surface area and light harvesting of the micropillar arrays, achieving a 3 times increase in photocurrent density at 1.5 V vs Ag/AgCl compared to smooth WO_3 coated micropillar arrays[24]. In all cases, the authors attribute the increased performance to the increased surface area and the enhanced light absorption.

Summarizing all studies on nano-/microstructured electrodes, it is found that the photocurrent enhancement is quite low regarding the highly enlarged surface area and enhanced light harvesting. For nanostructured photoelectrodes, which are closed to the scale of the wavelength of light, nanophotonic effects have been studied to intensify light in the photocatalytic[24–27]. For microstructured photoelectrodes, the situation is different because they behave very much like the ray optics case. Increased surface area and decreased light reflection contribute to the PEC performance as described in the literature. However, it has not been systematically studied how much surface is really active during the PEC reaction and how this active surface area is related to the geometry of the microstructured electrodes. Aiming at these questions, and in order to provide guidance to design highly efficient photoelectrodes in the future, we focus this study on well-defined micropillar array structures coated with PEC active material. We select WO_3 as the functional layer due to its high electron mobility (~12 $cm^2V^{-1}s^{-1}$ at room temperature) and suitable band-gap (2.6-2.9 eV)[12,28]. We fabricate n-type Si and radial p-n junction Si micropillar arrays as substrates to prepare WO_3/n-Si and WO_3/pn-Si micropillar array photoelectrodes. We systematically change the micropillar structure with pillar heights (10 μm and 40 μm) and pillar pitches (6 μm, 10 μm, 15 μm and 20 μm). These well-defined geometries allow for a quantitative study of the relation between surface area and PEC activity. It also allows to evaluate the importance of large surface area vs. high aspect ratio regarding optimized photoelectrode design. Furthermore, optical simulations are for the first

time carried out to study the intensity distribution of light incident on the pillar array surface. It contributes to illustrate the relation between the active surface area, i.e. the surface area under illumination, and the 3D geometry of the microstructured PEC electrodes.

This research establishes a relation between the geometry of photoelectrodes and the PEC performance. It can be used to predict performance and provide guidelines for designing high performance photoelectrodes.

2. Results and Discussion

Figure 1 shows the scanning electron microscopy (SEM) images of Si micropillar arrays coated with WO_3 after annealing in Ar. Well-defined and homogeneous micropillar arrays with different pillar length, 10 μm (Figure 1a) and 40 μm (Figure 1b) are fabricated. As shown in Figure 1c, the diameter of each single pillar is 4 μm. A detailed look at the wall of the pillars shows a pancake morphology (Figure 1c), which is due to the Si reactive ion etching process. Figure 1d and 1e show FIB cross-sectional SEM images from the top to the bottom of a single pillar. The bright and the dark part correspond to the WO_3 and the Si, respectively. The pillars are fully covered by WO_3 from top (Figure 1d) to bottom (Figure 1e). The crystalline structure of the WO_3 was determined by Grazing Incidence X-ray diffraction (GIXRD). As shown in Figure S1, the diffraction peaks of the WO_3 (black pattern) agree well with monoclinic WO_3 (JCPDS No. 83-0950), indicating that monoclinic WO_3 is obtained from the amorphous WO_3 (as deposited, red pattern) after annealing in Ar. The average crystallite size in vertical direction d was calculated from the XRD pattern (black) width using the Scherrer equation, d $= 0.9 \, \lambda / (\beta \cos \theta)$, where λ is the X-ray wavelength ($\lambda = 1.54060$ Å), β is the full width at half-maximum (fwhm) of the diffraction peak, and θ is the diffraction angle. The vertical crystallite size was calculated from the fwhm of the [002] peak and resulted in an average vertical size of 19.2 nm. The chemical composition of the WO_3 films which were prepared using the same method as in our earlier studies, has been investigated by XPS in our previous work[29]. No

4

impurity elements were found in the detection limit. For the oxidation state of W after annealing in a protective gas environment, 85.9% W^{6+} and 14.1% W^{5+} were found, which suggested the existence of oxygen vacancies in WO_3. The results showed that excess amounts of chemical defects can act as recombination centers which inhibit the electron transfer, thus decreasing the photocurrent generation. In the present work, all WO_3 films were fabricated using a fixed recipe. Hence, the oxidation state of W should be similar for all electrodes and different PEC performance due to different oxygen vacancies is not seen here.

These results confirm that well-defined WO_3/n-Si micropillar array photoanodes are fabricated, allowing a quantitative analysis on the relation of PEC activity and the electrode geometry.
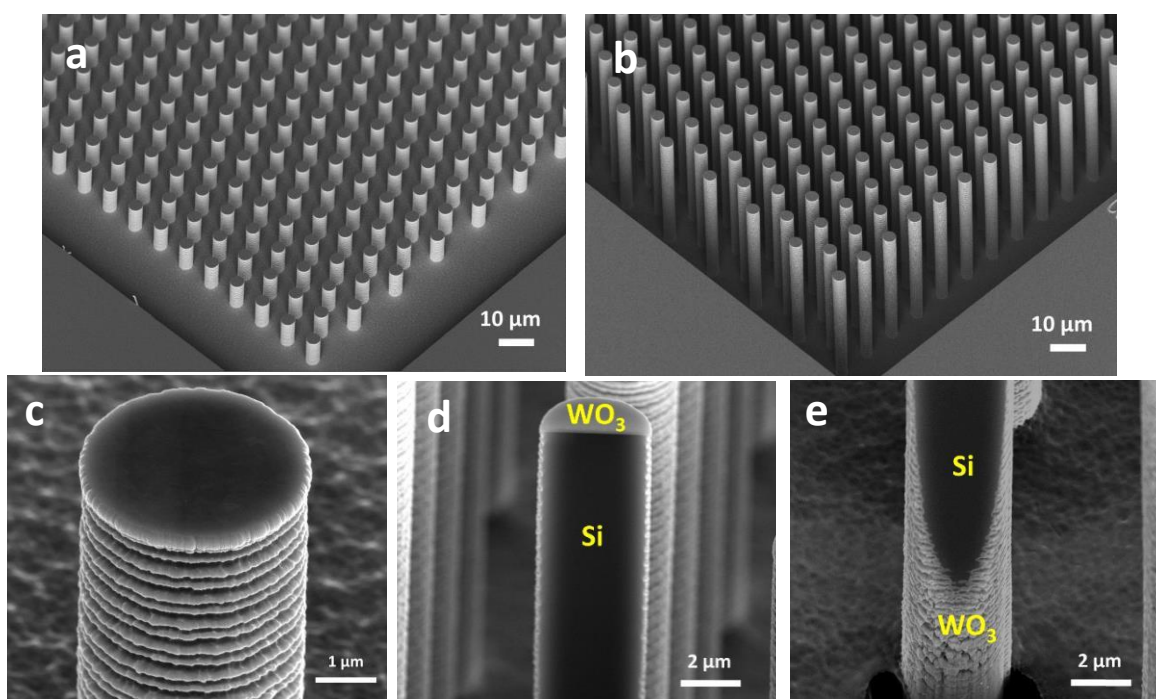

Figure 1. Scanning Electron Microscopy (SEM) images of micropillar arrays coated with WO_3 (a) 10 μm in height, 6 μm pitch, (b) 40 μm in height, 6 μm pitch (c) close view of single pillar, (d) and (e) cross-sectional FIB cut from the top (d) and the bottom (e) of a single pillar.

2.1 The PEC activity of WO₃/n-Si micropillar arrays

The PEC activity of the WO_3/n-Si micropillar array electrodes is evaluated by the photocurrents as a function of the applied potential (0.4 - 1.6 V vs RHE), which were measured

in 0.5 M H_2SO_4 under continuous AM 1.5 illumination. The photocurrent density is defined as the measured photocurrent divided by the projected surface area. The photocurrent densities obtained from two micropillar array electrodes with different pillar height are shown in **Figure 2**a. The 10 μm height micropillar array electrode shows a photocurrent density of 0.13 mA/cm^2 at 1.23 V vs RHE (blue curve). This is more than twice as high as the photocurrent density of 0.06 mA/cm^2 at 1.23 V vs RHE obtained for the planar electrode (purple curve). The photocurrent densities of the sputtered WO_3 films (200 nm) in this work are comparable to the literature. For planar sputtered WO_3 films, the photocurrent densities vary between 0.02 and 0.1 mA/cm^2 at 1.23 V vs RHE. The thicknesses of these reported WO_3 films vary from 50 to 500 nm [29–33]. When the pillar height increases to 40 μm (same pillar pitch), the photocurrent density increases to 0.17 mA at 1.23 V vs RHE. To further investigate the relation between PEC activity and the geometry of the electrode, we fabricated micropillar array electrodes with various pillar pitches (SEM images in Figure S2). Figure 2b shows the PEC activity of the micropillar array electrodes with various pillar pitches. The photocurrent density increases with the reduced pillar pitch: 0.08 mA/cm^2 (20 μm pitch), 0.1 mA/cm^2 (15 μm pitch), 0.13 mA/cm^2 (10 μm pitch) and 0.17 mA/cm^2 (6 μm pitch) at 1.23 V vs RHE.

The enhancement of the photocurrent density from the microstructured electrodes is attributed to two reasons. One is that the microstructure enhances light harvesting by reducing the light reflectance[34–36]. In the wavelength range below 400 nm, in which the light is absorbed by the functional layer WO_3[29], the reflectance of micropillar array electrodes, with 10 μm height and 40 μm height, decreased around 10% and 15%, respectively, compared with the planar electrode (Figure S2a). In addition, for micropillar arrays with different pillar pitch, the reflectance slightly decreases as the pillar pitch reduces (Figure S2b). This is related to the rough ground surface of the micropillar arrays which results in diffuse light reflection, and the reflected light is absorbed by the pillars.

Another reason for the photocurrent density enhancement from the micropillar structure compared to the planar is the increased number of catalytic sites due to the increased surface area. Quantitative relation between photocurrent density and surface area of the microstructure electrodes is so far not reported in the literature. It is, however, important to understand the geometrical limitations in designing photoelectrodes.

In this work, the well-defined geometry of the WO$_3$/n-Si micropillar arrays allows for a quantitative analysis to relate the surface area of the electrode to the PEC activity. The projected surface area of all the electrodes under illumination during PEC measurements are about 0.2 cm^2, which is determined by epoxy encapsulating and measured by image analysis. The total surface area of the micropillar array electrode, S$_{Total}$, can be calculated as

$$S_{Total} = S + \pi DH \times (\frac{S}{P^2}) = (1 + \pi \frac{DH}{P^2})S \tag{2}$$

where D is the diameter of the pillar, H is the height of the pillar, P is the pitch of the pillars, and S is the planar surface area; (Figure 2c). Figure 2d shows the photocurrent density at 1.23 V vs RHE (red curve) and the total surface area, S$_T$, (blue curve) for WO$_3$/n-Si micropillar arrays as a function of pillar pitch. Since the surface area of the planar electrode is defined as S, the total surface area of the micropillar array electrodes with different pillar pitch, 20 μm, 15 μm, 10 μm, and 6 μm, can be calculated according to Eq. (2) as 2.3 S, 3.2 S, 6.0 S and 15.0 S, respectively. Comparing the two curves in Figure 2d reveals that the increase in photocurrent density is less than the increase in total surface area, in particular when the pillar pitch reduces from 10 μm to 6 μm. This means that the photocurrent does not increase proportional with the total surface area. In other words, reducing pillar pitch, i.e. having the pillars closer together, increases the surface area, but the additional surface area is not fully electrochemically active.
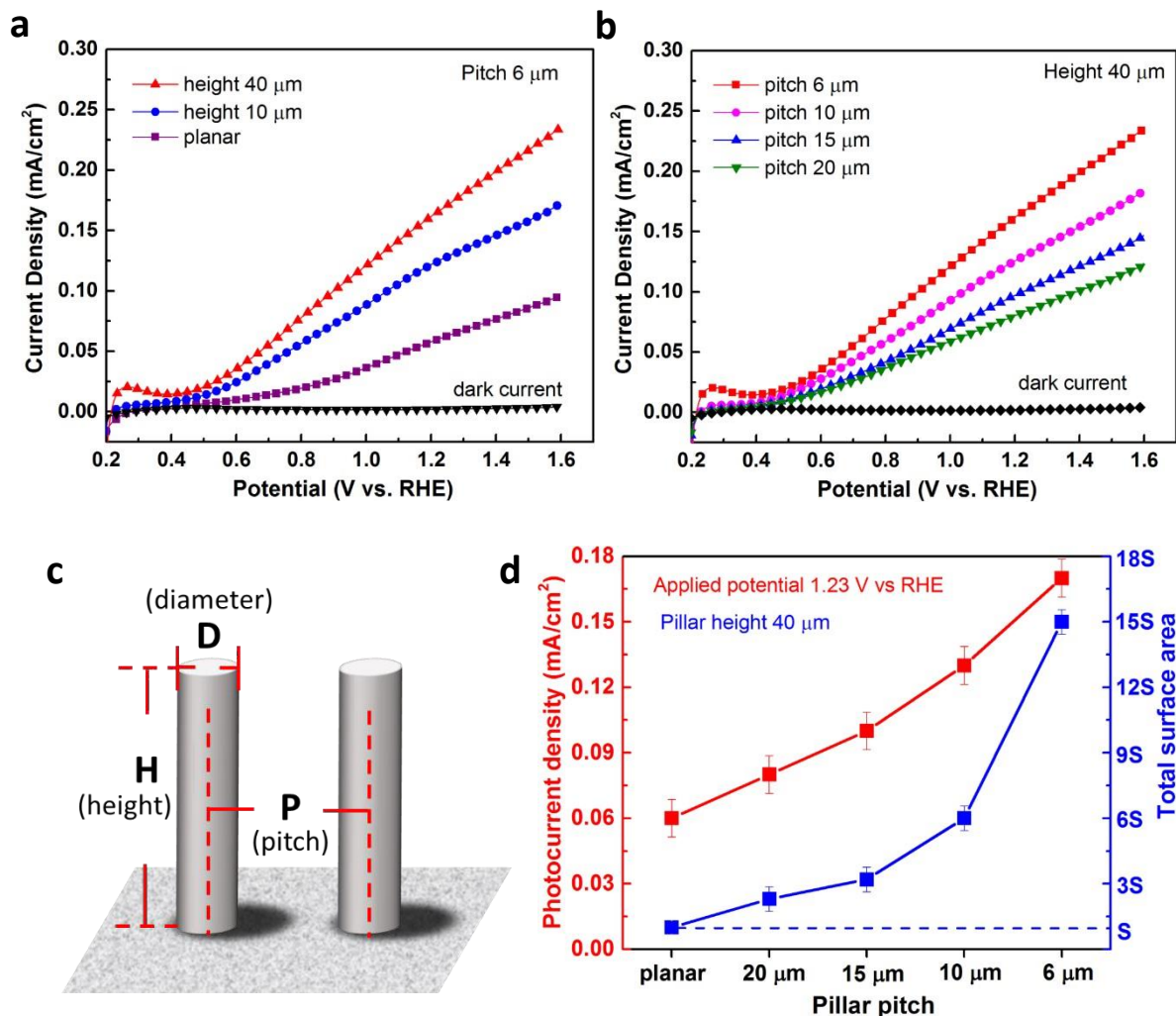
Figure 2. Photocurrent density vs applied potential curves under dark (black) and simulated sun light illumination (light intensity: 100 mW cm^{-2}; electrolyte: 0.5 M H$_2$SO$_4$) for WO$_3$/n-Si micropillar array electrodes with (a) different pillar height, 40 μm and 10 μm, and (b) different pillar pitch, 6 μm, 10 μm, 15 μm and 20 μm. (c) Dimensional sketch for surface area calculation. (d) Photocurrent densities at 1.23 V vs RHE (red) and total surface area, S$_T$, (blue) of micropillar arrays as a function of pillar pitch. The error bars denote the standard deviation of two different repetitive measurements in two different samples.

2.2 The PEC activity of WO$_3$/pn-Si micropillar arrays

To further improve the PEC activity, the n-Si micropillar array was doped with boron to form a radial p-n Si junction array. The sketch of the fabricated WO$_3$/pn-Si micropillar array photoelectrode is shown in **Figure 3**a. It should be noted that the WO$_3$/n-Si heterojunction can create a photovoltage due to the different Fermi levels of n-Si and WO$_3$.[32] In addition, the Fermi level of highly doped p-Si layer is between the Fermi levels of n-Si and WO$_3$. Theoretically, the created photovoltage from the WO$_3$/pn-Si should be the same as from the

WO$_3$/n-Si. However, the WO$_3$/n-Si heterojunction causes more recombinations of photogenerated carriers due to defects at the interface of between Si and WO$_3$, which can result in a lower photovoltage than a homojunction, i.e. p-n junction in Si. Moreover, the introduced tandem p-n junction in Si can more efficiently utilize the light penetrated from the WO$_3$. The created photovoltage can provide driving force for the charge transport during PEC water splitting. Figure 3b shows the working schematic of the p-n junction micropillar arrays under illumination during PEC process. Under illumination, the Si (band gap 1.1 eV[19]) absorbs the light that is penetrating through the WO$_3$ layer (band gap 3.0 eV[29]), and it results in photogenerated electrons and holes in both the Si and the WO$_3$. The photogenerated holes in the p-Si and the photogenerated electrons in the WO$_3$ migrate to the interface of p-Si and WO$_3$ and recombine in a so-called Z-scheme[6,23] In the meantime, the photogenerated holes in the WO$_3$ are driven to the WO$_3$/electrolyte interface for water oxidation. Under illumination, the introduced p-n junction in Si creates a photovoltage (ΔV_{pn-Si}, Figure 3b). This photovoltage can provide a driving force for the photogenerated carrier transport in the Z scheme system and thus enhances the PEC water splitting performance.[32,34] The photocurrent densities of the WO$_3$/pn-Si micropillar array electrodes with different pillar pitch are shown in Figure 3c. Compared with WO$_3$/n-Si (Figure 2), the WO$_3$/pn-Si junction reduces the onset potential, which is lower than 0.2 V vs RHE. In addition, the photocurrent densities of WO$_3$/pn-Si are significantly higher than those of WO$_3$/n-Si at low applied potential (0.2-1.2 V vs RHE). This improvement is due to the photovoltage created by the p-n junction in Si. While at higher applied potential, the photocurrent densities are similar for WO$_3$/pn-Si and WO$_3$/n-Si micropillar arrays. This is because the higher applied potential compensates for the lack of the driving force for electron transport in the WO$_3$/n-Si. In other word, at high applied potential, the limitation of the PEC performance is the amount of photogenerated charges instead of the charge transport. Therefore, the improvement of the photocurrent density in going from WO$_3$/n-Si to WO$_3$/pn-Si is smaller.

Particularly, when the applied potential increases to 1.6 V vs RHE, the photocurrent of WO_3/pn-Si structures with small pillar pitch (i.e. 6 μm) is even lower than that of the WO_3/n-Si structures without p-n junction. This can be attributed to the dead layer arising from the heavily p-doped surface of Si,[37] which causes increased recombination of the photogenerated carriers.

To further quantitatively evaluate the effect of the microstructure geometry on the photocurrent enhancement of the WO_3/pn-Si micropillar arrays, Figure 3d illustrates the relation between the photocurrent densities at a lower applied potential (0.8 V vs RHE) and the total surface area as a function of the pillar pitch. The photocurrent densities of WO_3/pn-Si micropillar array electrodes increase first and then decrease as the pillar pitch decreases. As shown in the Figure 3d (red curve with open symbol), the photocurrent density increases from 0.14 mA/cm^2 to 0.16 mA/cm^2, when the pillar pitch reduces from 20 μm to 15 μm. However, when the pillar pitch further reduces to 10 μm, and 6 μm, the photocurrent density decreases to 0.13 mA/cm^2, and 0.12 mA/cm^2, respectively. This trend is different for the WO_3/n-Si (red curve with filled symbol), which keeps increasing as the pillar pitch decreases, albeit at much slower increasing rate than the increased total surface area (blue curve). The photocurrent enhancements from the p-n junction for the WO_3/pn-Si micropillar arrays with different pillar pitch are 0.11 mA/cm^2 (20 μm), 0.12 mA/cm^2 (15 μm), 0.07 mA/cm^2 (10 μm) and 0.05 mA/cm^2 (6 μm). The enhancement at this relatively low applied potential (0.8 V vs RHE) benefits from the generated photovoltage by the p-n junction. Therefore, these results indicate that the photovoltage created by the p-n junction varies with the pillar pitch. This can be due to the dead layer caused by the heavily p-doped surface of the Si. When the pillar pitch is reduced to increase the surface area, the dead layer is increased and locks more absorbed photons. As a result, the function of the p-n junction below the dead layer in the Si is limited by the lack of photons.
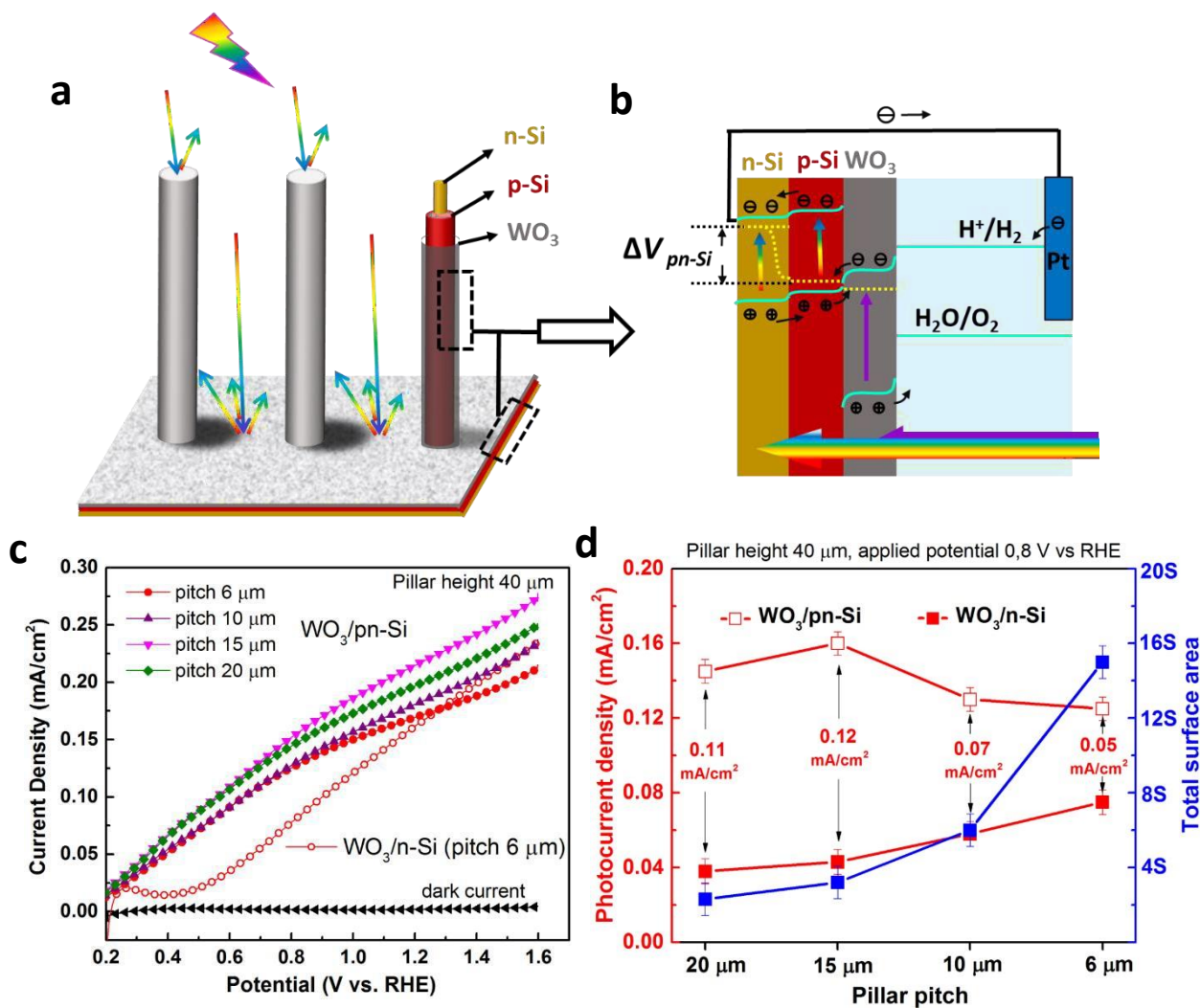
Figure 3. (a) Sketch of the WO$_3$/pn-Si micropillar array photoelectrodes. (b) Schematic illustration of the band diagrams of WO$_3$/pn-Si micropillar array photoelectrodes under illumination. (c) Photocurrent density vs. applied potential curves of WO$_3$/pn-Si micropillar arrays with 40 μm pillar height, and different pillar pitch, 6 μm, 10 μm, 15 μm and 20 μm. (d) Photocurrent densities at 0.8 V vs RHE (red) and total surface area (blue) of WO$_3$/n-Si and WO$_3$/pn-Si micropillar arrays with different pillar pitch. The error bars denote the standard deviation of two different repetitive measurements in two different samples.

To evaluate the relation between the photovoltage and the pillar pitch, we carried out V$_{OC}$ measurements for the WO$_3$/pn-Si micropillar arrays under chopped monochromatic IR illumination. The idea is that due to the different bandgaps of Si (~1.1 eV[19]) and WO$_3$ (~3.0 eV from our previous work[29]), the Si can be excited selectively by IR illumination (wavelength, 980 nm), which allows obtaining the decoupled photovoltage from the pn-Si only. Under IR illumination, electron–hole pairs are generated in Si only. The holes migrate toward the interface with WO$_3$ in the built-in field and partly recombine with available electrons in the

11

WO$_3$. Therefore, the Fermi level (E$_F$) in n-Si shifts upwards and in WO$_3$ shifts downwards, resulting in a more cathodic V$_{OC}$. The photovoltage created in the circuit can be determined by the change of the open circuit potential (V$_{OC}$) under illumination.[32] As shown in **Figure 4**, under chopped IR illumination, the V$_{OC}$ shows a cathodic shift of 0.47 V, 0.50 V, 0.6 V and 0.57 V, for the WO$_3$/pn-Si micropillar arrays with pillar pitch of 6 μm, 10 μm, 15 μm, and 20 μm, respectively. The amounts of the created photovoltage are according to the amounts of the photocurrent enhancements for the WO$_3$/pn-Si micropillar arrays with different pillar pitch (Figure 3d). These results also support that the reduced pillar pitch increases the dead layer which leads to a reduced photovoltage created by the p-n junction.
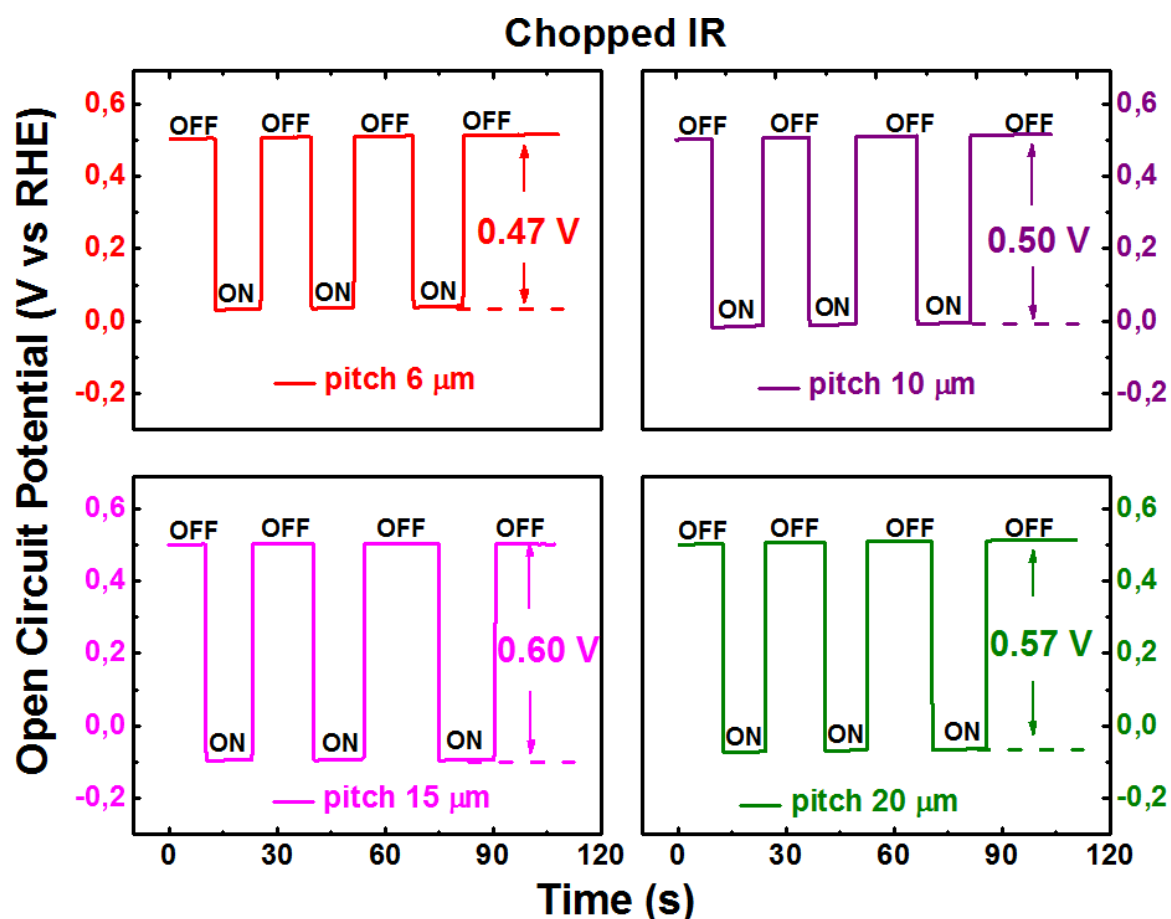
Figure 4. Open circuit potential (V$_{OC}$) versus elapsed time for WO$_3$/pn-Si micropillar arrays with different pillar pitch under chopped IR (λ = 980 nm) illumination (electrolyte: 0.5 M H$_2$SO$_4$).

2.3 Optical simulations

The activity of the WO$_3$ on the micropillars is also influenced by the accepted light intensity under illumination, which is related to the 3D geometry of the microstructure. Unlike nanostructured photoelectrodes, in which the nanophotonic effects come into play[24–27], the microstructured photoelectrodes behave mostly like the ray optics case. Under experimental conditions, the light incident angle is usually not exactly 0°. Therefore, shadowing effects can result in surface area with lower light intensity under illumination, as shown in **Figure 5**. It should be pointed out that the light penetration depth in Si is a function of light wavelength, which is ≤100 nm for the light below ~400 nm.[38] As a results, with a band gap of ~3.0 eV, the WO$_3$ located at the shadowed area cannot be excited by the light penetrated through the Si. Therefore, the PEC activity of the WO$_3$/Si micropillar array electrodes are influenced by the incident light fallen on the WO$_3$ surface area (including the reflected light).
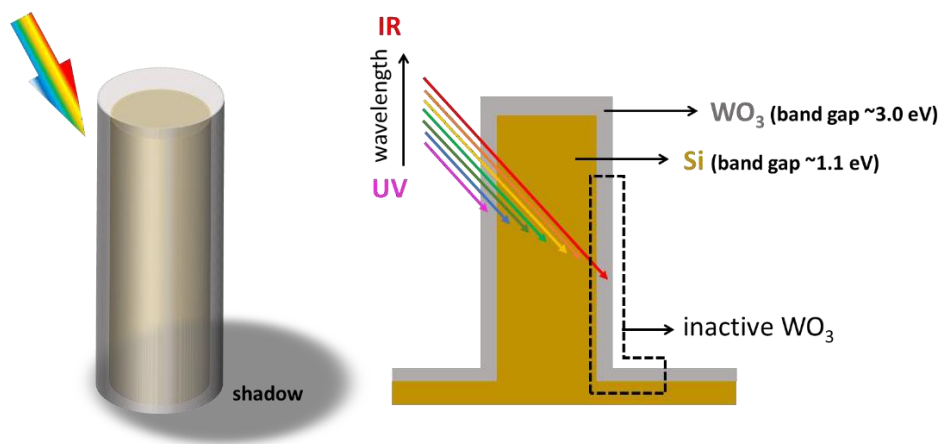
Figure 5. Sketch of the WO$_3$/Si micropillar under illumination.

To evaluate the relation between the light incident surface area and the geometry of the micropillar electrodes, we carried out optical simulations using the ray-tracing software LUX (developed at TU Delft), which can determine the intensity distribution of the light illuminated on the surface of micropillar arrays (including the reflected light). The details of the simulation methods are described in experimental section 2.5. **Figure 6**a shows the relative incident intensity distribution map of light illuminated on simulated "metallic-like", i.e. no light

13

transmission, micropillar arrays with different pillar pitch using a small incident angle of 1°. It can be seen that the flat area including the pillars top and the floor are illuminated with a higher light intensity. The wall surface of the pillars, on the other hand, is illuminated with a lower light intensity. In addition, the shadowing of the pillars appears on the floor, and the shadowing area increases as the pillar density increases, i.e. as the pillar pitch is reduced. Particularly, when the pillars pitch is reduced to 6 μm, the shadowing of the pillars is even casted on the adjacent pillars, not only on the floor. Figure 6b demonstrates the relation between the light illuminated area and the pillar pitch for different incident angles. Note that we consider an area to be 'illuminated' when it receives an irradiance that is at least 0.2 of the incident beam normal irradiance (in W/m^2). It shows that the high intensity light illuminated area decreases with the reduced pillar pitch. This decrease becomes larger when the incident angle increases from 1° to 10°. The optical simulation results confirm that the reduced pillar pitch increases the total surface area of the photoelectrode, but at the same time decreases the factional area that is actually illuminated. The correspondingly larger shadowed area means that a larger fraction of the surface is inactive for the PEC reaction. This could explain that the photocurrent density increases much slower than the total surface area with reduced pillar pitch of the WO_3/n-Si micropillar arrays (Figure 2d).
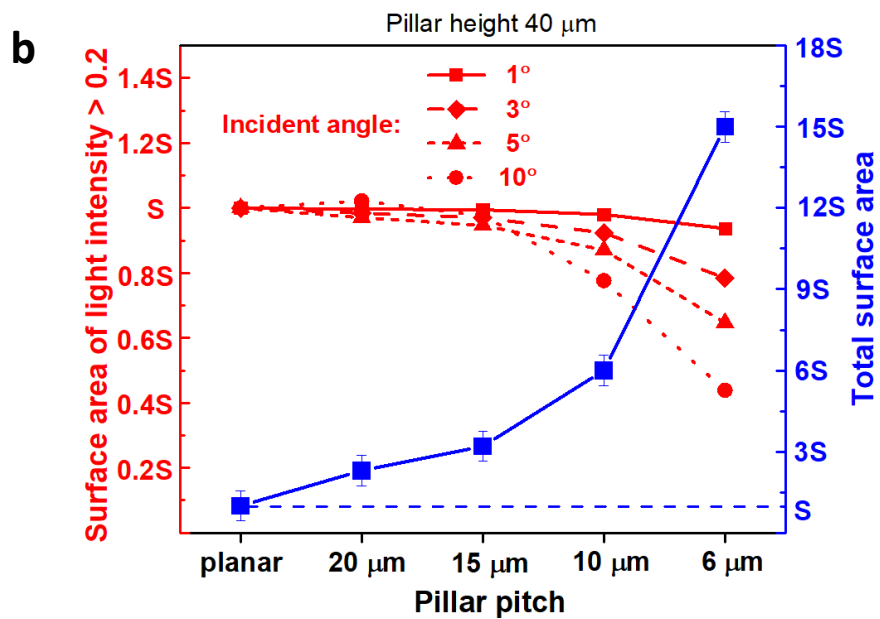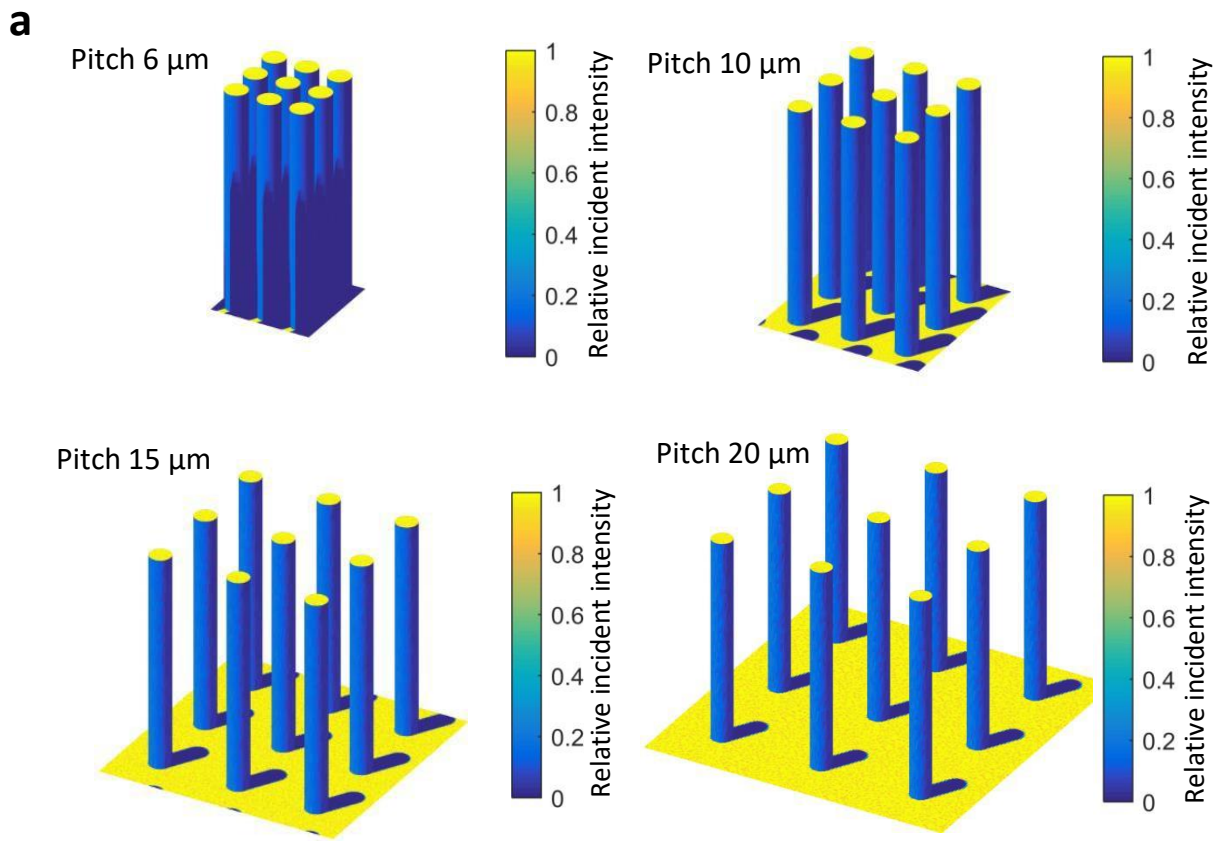
Figure 6. (a) Optical simulations of the intensity distribution map of light illuminated on "metallic" micropillar arrays with different pillar pitch, 6 μm, 10 μm, 15 μm, and 20 μm. (Pillar height 40 μm; light incident angle 1°). (b) Optical simulation results of the total surface area with area of light intensity >0.2 under different incident angle (red curve), and the total surface area (blue curve) for micropillar arrays with different pillar pitch.

Based on the discussion above, instead of just increasing the total surface area by pursuing high aspect ratio, the geometry needs to specifically enlarge the illuminated area for the 3D microstructure photoelectrode design. Here, to reduce the shadowing effects, we suggest a micro-cone design for high performance microstructured photoelectrodes for water splitting, as shown in **Figure 7**a. Optical simulations are carried out to demonstrate the light density under illumination of the micro-cone array structure. Figure 7b illustrates the light intensity map of the micro-cone arrays under illumination at an incident angle of 1°. Compared to the micropillar arrays (Figure 5a), there are no obvious shadowing areas on the ground or on the wall surface of the cone-shapes. In addition, the light density on the wall surface of the micro-cones is higher than that for the micropillar array structure.
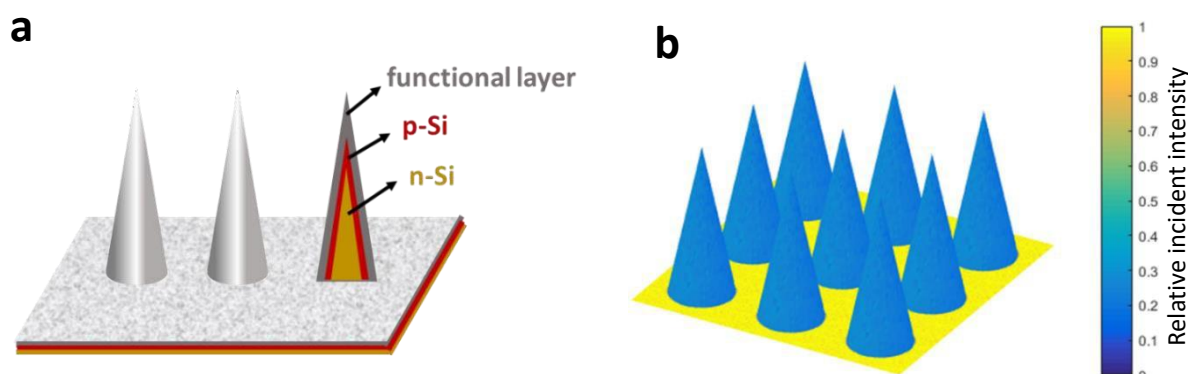
Figure 7. (a) A promising cone-shape micro structure with p-n junction. (b) Optical simulation of the light intensity map of the cone-shape micro structure under illumination (light incident angle 1°).

3. Summary and Conclusion

Well-defined Si micropillar arrays are prepared on Si wafers using photolithography and deep reactive ion etching. The fabricated WO_3/n-Si micropillar array electrodes show up to 3 times enhancement of the photocurrent density at an applied potential of 1.23 V vs RHE in PEC water splitting. In order to further increase the performance at low applied potential, a radial p-n junction is introduced using boron doping of the n-Si micropillar arrays; the p-n junction can provide a photovoltage that benefits the electron transport. Indeed, an up to 4 times

higher photocurrent density was achieved at low potential (0.8 V vs RHE) for the WO_3/pn-Si micropillar array electrodes compared to the WO_3/n-Si electrodes.

The well-defined micro-structure allows for quantitative study of the relation between the PEC performance and the electrode geometry. The results reveal that the PEC activity does not show a linear relation with the increased surface area resulting from an increased pillar length or a reduced pillar pitch. Optical simulations of the intensity distribution resulting from illumination at various incident angles reveal that the reduced pillar pitch, i.e. having the pillars closer together, decreases the fraction of highly illuminated area. Any area with low light intensity, i.e. shadowed area, is inactive surface area for the PEC reaction. This can be a reason for the small increase in photocurrent density compared to the large increase in total surface area in WO_3/n-Si micropillar arrays. Based on the results, we propose a promising micro-cone array structured photoelectrode. Optical simulations demonstrate that this structure can reduce the shadowing effects under illumination.

In the case of WO_3/pn-Si micropillar arrays, the photocurrent density increases first and then decreases, when the pillar density is increased. By measuring the open circuit potential under chopped monochromatic IR illumination, it is proven that the photocurrent density enhancement in WO_3/pn-Si micropillar arrays is dominated by the photovoltage created at the p-n junction. However, with reduced pillar pitch, the increased surface area also causes increased dead layer, i.e. the heavily p-doped Si surface, which reduces the created photovoltage by the p-n junction, and therefore causes a decreased enhancement on the photocurrent density.

This research provides a deeper understanding of the effect of 3D geometry on the PEC performance using well-defined WO_3/n-Si and WO_3/pn-Si micropillar arrays. The well-defined geometry of the electrodes allows for the first time relating light density distribution and

microstructure geometry of the photoelectrode, thereby expressing how this relation has impact on the PEC performance. In general, this work shows the potential of using Si processing for tailored design of 3D nano-/microstructure and for high performing electrodes.

4. Experiments Section

Fabrication of n-Si and pn-Si micropillar arrays: The n-type Si (n-Si) and p-n junction Si (pn-Si) micropillar arrays were fabricated as previously reported[39,40] and the fabrication process is shown schematically in **Figure 8**. In summary, n-type Si {100} (1–10 Ω cm, 100 mm diameter, 375 μm thickness, single side polished, Cz-grown, Okmetic Finland) were cleaned and covered with 100 nm silicon-rich silicon nitride (SiN$_x$) via low-pressure chemical vapor deposition (LPCVD). On the polished side, the SiN$_x$ was removed by reactive ion etching (RIE, Adixen AMS100DE) and cleaned by means of oxygen plasma (30 min) and piranha (mixture of sulfuric acid and 30% aqueous hydrogen peroxide, 3:1 (v/v), 20 min). By means of standard photolithography (Olin 907-17 photoresist), the substrate was patterned with arrays of hexagonally packed dots (4 μm diameter, 6 μm, 10 μm, 15 μm and 20 μm pitch, 0.5 × 0.5 cm^2 squares on a specimen of 2 cm × 2 cm). This pattern was transferred into the silicon by deep reactive ion etching (CF-chemistry, Adixen AMS100SE). The height of the pillar arrays was controlled by the etching time, where the etching rate of silicon was about 3.2 μm min^{-1}. The substrates were cleaned subsequently in oxygen plasma (30 min) and piranha (20 min) to remove the photoresist and fluorocarbon residues.

The radial np junction was formed by a solid source doping of boron. The wafers were cleaned in room temperature 99% nitric acid, 95°C 69% nitric acid and 1% aqueous HF solution subsequently, rinsed thoroughly in DI water between each step, and finally dried. They were then placed in a furnace with the top side of the wafer facing (but not touching) a boron nitride wafer which served as a source of boron. A layer of boron oxide was grown on the wafers at 900°C in an atmosphere of 2 standard liters per minute (SLM) N$_2$ and 2 SLM O$_2$ for 15 min,

and the atmosphere was changed to only N_2 (4 SLM) and the temperature of the furnace was further increased to 1050℃. It remained in that condition for 15 min to diffuse the boron from the boron oxide into the silicon, and then it was cooled down again and removed from the furnace. After the thermal diffusion step, the boron oxide was removed by immersion in BHF (NH 4 F-buffered aqueous HF) for 10 min, and the silicon nitride from the backside of the substrate was stripped in 50% aqueous HF (30 min).
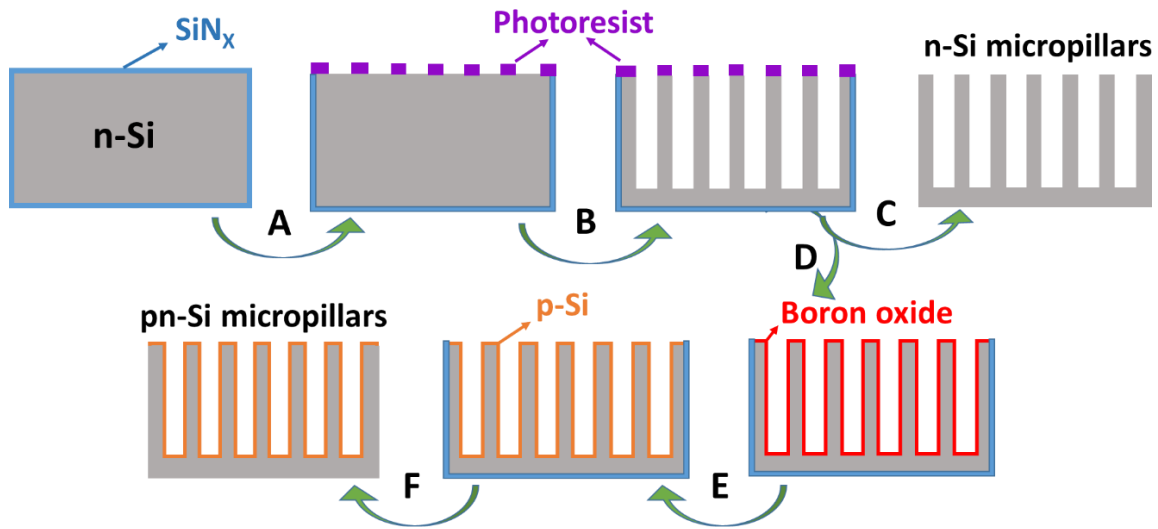
Figure 8. Schematic fabrication process of n-Si and pn-Si micropillar arrays. (A) Removal of topside silicon nitride (SiN_x) followed by photolithography. (B) Deep reactive ion etching of Si. (C) Removal of photoresist and SiN_x. (D) Boron oxide deposited from solid source. (E) Formation of the radial junction, by a drive-in step at 1050 °C for 15 min. (F) Removal of SiN_x.

WO₃ films fabrication: The Si micropillar arrays were cleaned sequentially in an ultrasonic bath of isopropanol and distilled (DI) water each for 20 min before WO₃ deposition. WO₃ films were deposited by reactive RF sputtering with a Bestec GmbH sputter tool using a 2 in. metallic tungsten target (Karl Jesko, purity 99.95%) with a target−substrate distance of ∼100 mm. The gas mixture was 40/10 sccm Ar/O_2, where the O_2 is inserted at the sample position and the Ar at the W target. The main deposition parameters are listed in Table 1.

Table 1: Sputtering process parameters for WO₃ deposition.

Parameter	Value

Target power	100 W
Base pressure	$<10^{-8}$ mbar
Deposition pressure	10^{-2} mbar
Substrate temperature	Room temperature
O_2 flow rate	10 sccm
Ar flow rate	40 sccm

After deposition, all samples were annealed at 450°C in Ar for 1 h with a ramping rate of 5°C/min using a tubular furnace with a quartz tube (Carbolite Gero). The Ar gas flow was started 30 min prior to annealing to guarantee a stable gas atmosphere.

Characterizations: The morphologies of the micropillar array electrodes were investigated by a field emission scanning electron microscope (SEM) (Zeiss Sigma, Germany) with an in-lens detector and 5 kV accelerating voltage. Cross-sectional SEM sample preparation and imaging was performed using a focused ion beam (FIB) and the scanning electron microscope of the FIB/SEM Dualbeam (FEI, The Netherlands). A focused beam of 30 kV Ga-ions is used to cut a crater at normal angle of incidence into a surface. The crater wall is imaged with the SEM at 10 kV x 0.5 nA at an angle. For this setup the sample table is tilted to 52° to allow normal incidence for the ion beam. The scale bar corrects for the tilt in the SEM image to allow for correct dimensions on the crater wall. For cutting the micropillars no protection layer was used since the top was already protected with WO_3 layer of several hundred nanometers.

PEC measurements: A three-electrode PEC cell with a quartz window was used to measure the PEC performance at room temperature. Simulated sunlight illumination was performed by an AM 1.5 class A solar simulator (LCS 100, Oriel Instruments) using a 100 W Xe lamp with a calibrated illumination intensity of 100 mW cm^{-2} at the sample position. The

light source was calibrated with a calibrated reference cell and meter (Newport, model 91150 V). The monochromatic light illumination was carried out using an IR laser (λ = 960 nm, cw, 200 mW) as light source. The micropillar array electrodes (working electrodes) were encapsulated in epoxy (Loctite EA 9492) resulting in exposed micropillar array areas of about 0.2 cm^2. The exact geometrical area of the exposed electrode surface was determined by calibrated digital images and ImageJ software. For ohmic contact to the n-Si (backside of the electrodes), a drop of Ga/In eutectic (Sigma Aldrich) was used to contact the Si and a copper wire. A coiled Pt wire (0.8 mm diameter) and an Ag/AgCl/Sat. KCl electrode (XR 300, Radiometer Analytical) were used as the counter and reference electrode, respectively. An aqueous solution of 0.5 M H_2SO_4 (pH ~0.3) was used as electrolyte. The potential of the electrode was controlled with a BioLogic SP-150 potentiostat. All potentials reported in PEC results in this study are given versus reversible hydrogen electrode (RHE) through the relation[4]

$$\Phi_{RHE} = \Phi_{Ag/AgCl} + \Phi^o{}_{Ag\ AgCl\ vs\ RHE} + 0.059 \times pH \qquad (1)$$

with $\Phi^o{}_{Ag/AgCl}$ is 0.197 V versus RHE at 25°C. Linear sweep voltammetry (LSV) measurements were performed at potentials between 0.4 V and 1.6 V versus RHE at a scan rate of 10 mV s^{-1}.

Optical simulation: Optical simulations are performed to determine the intensity distribution of light on the micropillar arrays. The ray-tracing software LUX (developed at TU Delft) is used, which makes use of periodic boundary conditions. This allows for efficient three-dimensional simulation of an infinite array of pillars, taking into account all optical interactions, such as reflections and shading between all neighbouring pillars. It does so by considering one unit cell, containing a single pillar on a square base with periodic boundary conditions applied to the four side walls of the unit cell. The pillar and base are discretized into approximately 4000 surface elements. The top of the domain acts as the light source from which 10^5 parallel rays are emitted. The paths of all rays are traced efficiently using a parallelization algorithm. A

ray hitting a surface element is partly absorbed and partly reflected. The reflected light is given as a cosine-squared angular distribution. A ray can undergo multiple reflections until it is either fully absorbed or escapes the simulation domain at the top. After all rays have been traced, the intensity absorbed in each of the surface elements is obtained and normalized by dividing it by the intensity of the incident beam. A statistical analysis of these results reveals the number of surface elements and the corresponding surface area per unit cell that is illuminated (i.e. not shadowed).

Supporting Information
Supporting Information is available from the Wiley Online Library or from the author.

Received: ((will be filled in by the editorial staff))
Revised: ((will be filled in by the editorial staff))
Published online: ((will be filled in by the editorial staff))

Reference

[1]   A. Fujishima, K. Honda, *Nature* **1972**, *238*, 37.

[2]   K. Sivula, R. van de Krol, *Nat. Rev. Mater.* **2016**, *1*, 15010.

[3]   Nathan S. Lewis, *Science* **2016**, *351*, aad1920.

[4]   H. L. Tuller, *Photoelectrochemical Hydrogen Production*, Springer US, Boston, MA, **2012**.

[5]   X. Zhang, P. Klaver, R. Van Santen, M. C. M. Van De Sanden, A. Bieberle-Hütter, *J. Phys. Chem. C* **2016**, *120*, 18201.

[6]   Y. J. Hwang, A. Boukai, P. Yang, *Nano Lett.* **2009**, *9*, 410.

[7]   S. Kuang, L. Yang, S. Luo, Q. Cai, *Appl. Surf. Sci.* **2009**, *255*, 7385.

[8]   Y. Lin, Y. Xu, M. T. Mayer, Z. I. Simpson, G. McMahon, S. Zhou, D. Wang, *J. Am. Chem. Soc.* **2012**, *134*, 5508.

[9]   Y. Zhao, K. R. Yang, Z. Wang, X. Yan, S. Cao, Y. Ye, Q. Dong, X. Zhang, J. E. Thorne, L. Jin, K. L. Materna, A. Trimpalis, H. Bai, S. C. Fakra, X. Zhong, P. Wang, X. Pan, J. Guo, M. Flytzani-Stephanopoulos, G. W. Brudvig, V. S. Batista, D. Wang, *Proc. Natl. Acad. Sci. USA* **2018**, *115*, 2902.

[10]   J. Y. Zheng, G. Song, C. W. Kim, Y. S. Kang, *Nanoscale* **2013**, *5*, 5279.

[11]   K. Yuan, Q. Cao, X. Li, H. Y. Chen, Y. Deng, Y. Y. Wang, W. Luo, H. L. Lu, D. W. Zhang, *Nano Energy* **2017**, *41*, 543.

[12] C. A. Bignozzi, S. Caramori, V. Cristino, R. Argazzi, L. Meda, A. Tacca, *Chem. Soc. Rev.* **2013**, *42*, 2228.

[13]   D. Barreca, G. Carraro, A. Gasparotto, C. Maccato, T. Altantzis, C. Sada, K. Kaunisto, T. P. Ruoko, S. Bals, *Adv. Mater. Interfaces* **2017**, *4*, 1700161.

[14]   M. Li, L. Zhao, L. Guo, *Int. J. Hydrogen Energy* **2010**, *35*, 7127.

[15]   K. Sivula, F. Le Formal, M. Grätzel, *ChemSusChem* **2011**, *4*, 432.

[16]   W.-H. Hung, T.-M. Chien, C.-M. Tseng, *J. Phys. Chem. C* **2014**, *118*, 12676.

[17]   J. Ran, J. Zhang, J. Yu, S. Z. Qiao, *ChemSusChem* **2014**, *7*, 3426.

[18] Y. Yu, Z. Zhang, X. Yin, A. Kvit, Q. Liao, Z. Kang, X. Yan, Y. Zhang, X. Wang, *Nat. Energy* **2017**, *2*, 17045.

[19]   S. Y. Reece, J. a. Hamel, K. Sung, T. D. Jarvi, a. J. Esswein, J. J. H. Pijpers, D. G. Nocera, *Science* **2011**, *334*, 645.

[20] P. Leempoel, M. Castro-Acuna, F. R. F. Fan, A. J. Bard, *J. Phys. Chem.* **1982**, *86*, 1396.

[21] A. Kargar, S. J. Kim, P. Allameh, C. Choi, N. Park, H. Jeong, Y. Pak, G. Y. Jung, X. Pan, D. Wang, S. Jin, *Adv. Funct. Mater.* **2015**, *25*, 2609.

[22] S. Y. Noh, K. Sun, C. Choi, M. Niu, M. Yang, K. Xu, S. Jin, D. Wang, *Nano Energy* **2013**, *2*, 351.

[23] M. T. Mayer, C. Du, D. Wang, *J. Am. Chem. Soc.* **2012**, *134*, 12406.

[24] R. H. Coridan, K. a Arpin, B. S. Brunschwig, P. V Braun, N. S. Lewis, *Nano Lett.* **2014**, *14*, 2310.

[25] S. J. Kim, I. Thomann, J. Park, J. Kang, A. Vasudev, M. L. Brongersma, *Nnao Lett.* **2014**, *14*, 1446.

[26] Y. Qiu, S.-F. Leung, Q. Zhang, B. Hua, Q. Lin, Z. Wei, K. Tsui, Y. Zhang, S. Yang, Z. Fan, *Nano Lett.* **2014**, *14*, 2123.

[27] M. L. Brongersma, Y. Cui, S. Fan, *Nat. Mater.* **2014**, *13*, 451.

[28] T. Zhu, M. N. Chong, E. S. Chan, *ChemSusChem* **2014**, *7*, 2974.

[29] Y. Zhao, S. Balasubramanyam, R. Sinha, R. Lavrijsen, M. A. Verheijen, A. A. Bol, A. Bieberle-Hütter, *ACS Appl. Energy Mater.* **2018**, *1*, 5887.

[30] D. Valerini, S. Hernández, F. Di Benedetto, N. Russo, G. Saracco, A. Rizzo, *Mater. Sci. Semicond. Process.* **2016**, *42*, 150.

[31] T. Stoll, G. Zafeiropoulos, I. Dogan, H. Genuit, R. Lavrijsen, B. Koopmans, M. N. Tsampas, *Electrochem. commun.* **2017**, *82*, 47.

[32] Y. Zhao, G. Brocks, H. Genuit, R. Lavrijsen, M. A. Verheijen, A. Bieberle-Hütter, *Adv. Energy Mater.* **2019**, 1900940.

[33] M. B. Johansson, A. Mattsson, S. E. Lindquist, G. A. Niklasson, L. Österlund, *J. Phys. Chem. C* **2017**, *121*, 7412.

[34] M. R. Shaner, K. T. Fountaine, S. Ardo, R. H. Coridan, H. a. Atwater, N. S. Lewis, *Energy Environ. Sci.* **2014**, *7*, 779.

[35] W. Vijselaar, R. Elbersen, R. M. Tiggelaar, H. Gardeniers, J. Huskens, *Adv. Energy Mater.* **2017**, *7*, DOI 10.1002/aenm.201601497.

[36] W. Vijselaar, P. Westerik, J. Veerbeek, R. M. Tiggelaar, E. Berenschot, N. R. Tas, H. Gardeniers, J. Huskens, *Nat. Energy* **2018**, DOI 10.1038/s41560-017-0068-x.

[37] P. Kittidachachan, T. Markvart, G. J. Ensell, R. Greef, D. M. Bagnall, *Conf. Rec. IEEE Photovolt. Spec. Conf.* **2005**, *5*, 1103.

[38] M. A. Green, M. J. Keevers, *Prog. Photovoltaics Res. Appl.* **1995**, *3*, 189.

[39] R. Elbersen, R. M. Tiggelaar, A. Milbrat, G. Mul, H. Gardeniers, J. Huskens, *Adv. Energy Mater.* **2015**, *5*, 1401745.

[40] W. Vijselaar, P. Westerik, J. Veerbeek, R. M. Tiggelaar, E. Berenschot, N. R. Tas, H. Gardeniers, J. Huskens, *Nat. Energy* **2018**, DOI 10.1038/s41560-017-0068-x.
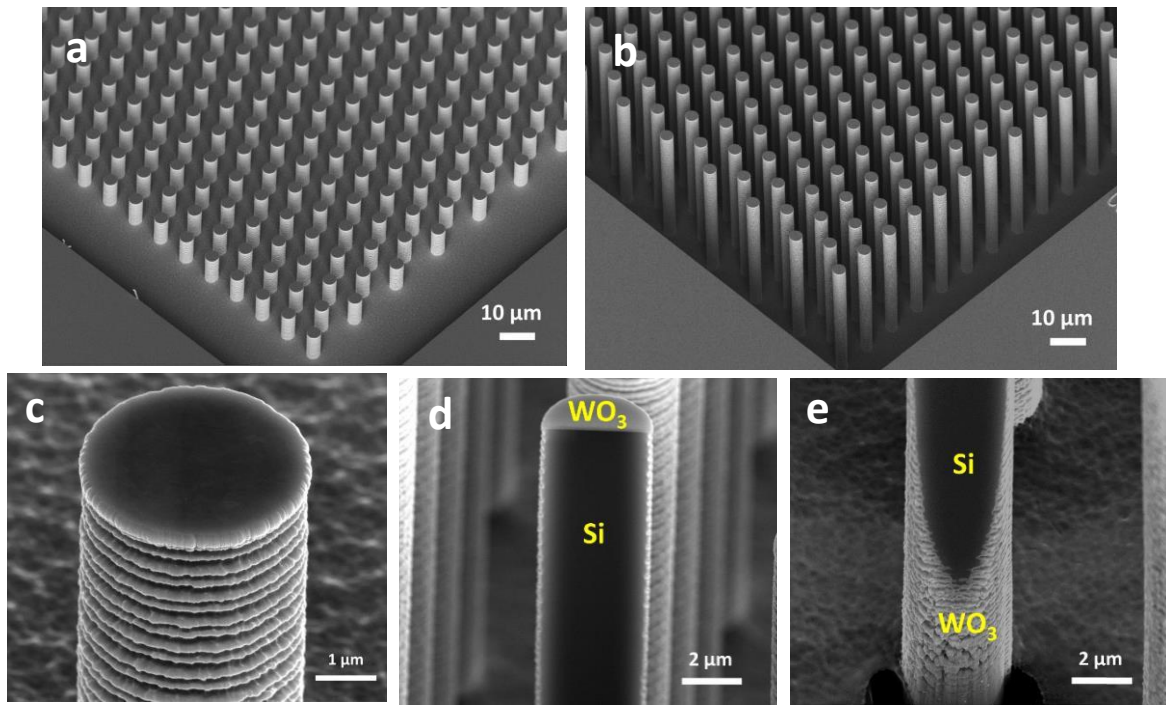
Figure 1. Scanning Electron Microscopy (SEM) images of micropillar arrays coated with WO_3 (a) 10 μm in height, 6 μm pitch, (b) 40 μm in height, 6 μm pitch (c) close view of single pillar, (d) and (e) cross-sectional FIB cut from the top (d) and the bottom (e) of a single pillar.

Figure 2. Photocurrent density vs applied potential curves under dark (black) and simulated sun light illumination (light intensity: 100 mW cm^{-2}; electrolyte: 0.5 M H$_2$SO$_4$) for WO$_3$/n-Si micropillar array electrodes with (a) different pillar height, 40 μm and 10 μm, and (b) different pillar pitch, 6 μm, 10 μm, 15 μm and 20 μm. (c) Dimensional sketch for surface area calculation. (d) Photocurrent densities at 1.23 V vs RHE (red) and total surface area, S$_T$, (blue) of micropillar arrays as a function of pillar pitch. The error bars denote the standard deviation of two different repetitive measurements in two different samples.
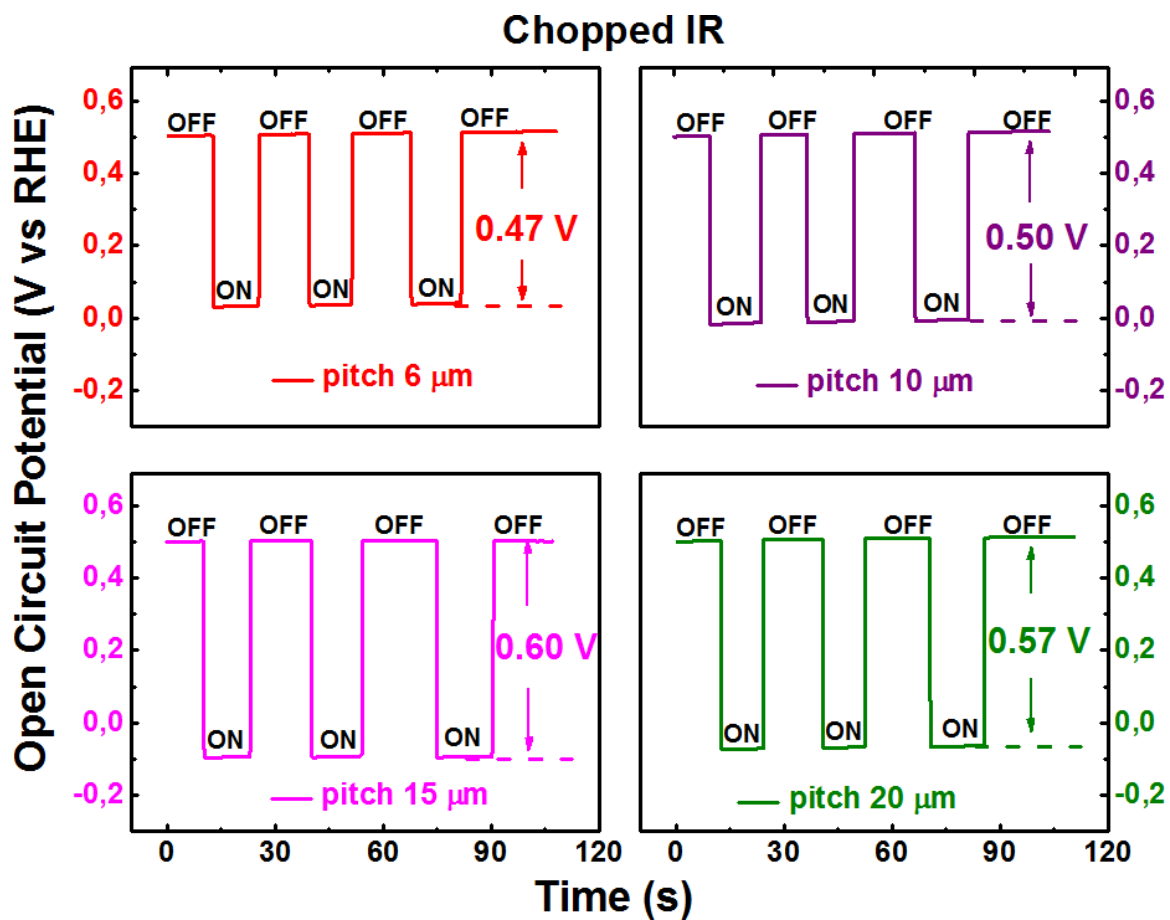
Figure 3. (a) Sketch of the WO$_3$/pn-Si micropillar array photoelectrodes. (b) Schematic illustration of the band diagrams of WO$_3$/pn-Si micropillar array photoelectrodes under illumination. (c) Photocurrent density vs. applied potential curves of WO$_3$/pn-Si micropillar arrays with 40 μm pillar height, and different pillar pitch, 6 μm, 10 μm, 15 μm and 20 μm. (d) Photocurrent densities at 0.8 V vs RHE (red) and total surface area (blue) of WO$_3$/n-Si and WO$_3$/pn-Si micropillar arrays with different pillar pitch. The error bars denote the standard deviation of two different repetitive measurements in two different samples.

Figure 4. Open circuit potential (V_{OC}) versus elapsed time for WO_3/pn-Si micropillar arrays with different pillar pitch under chopped IR (λ = 980 nm) illumination (electrolyte: 0.5 M H_2SO_4).
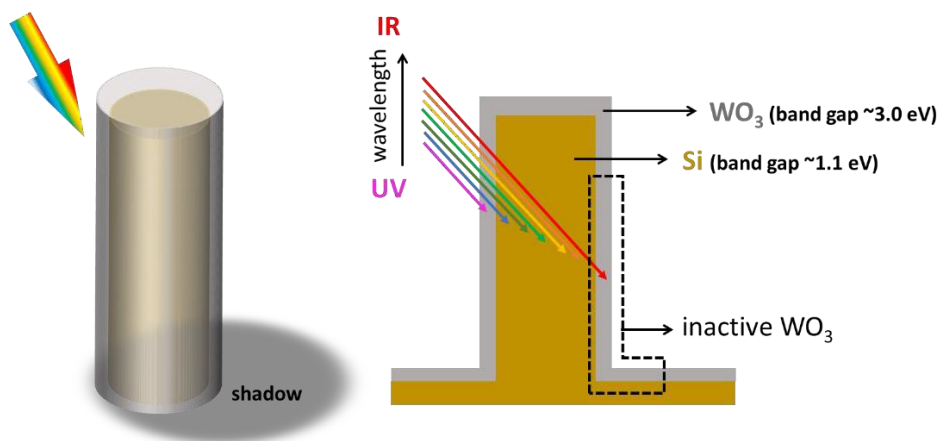
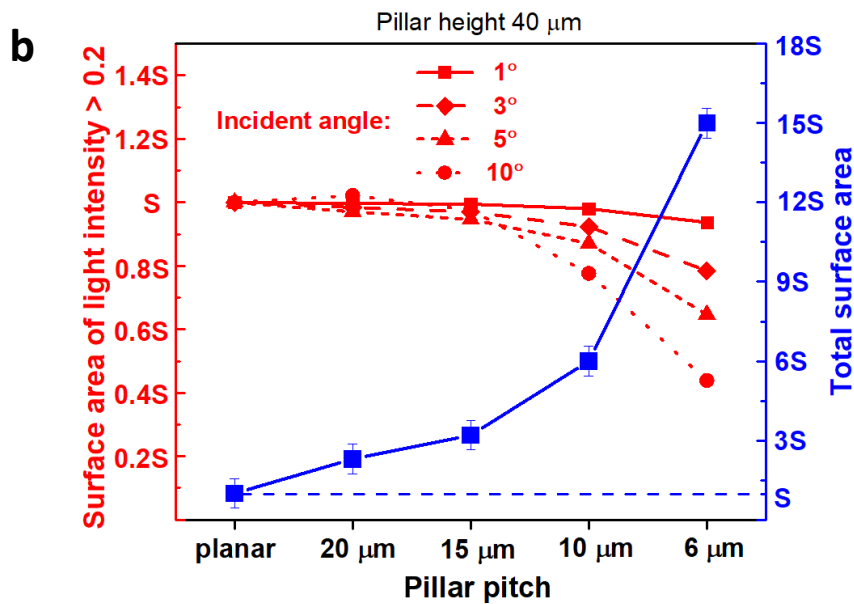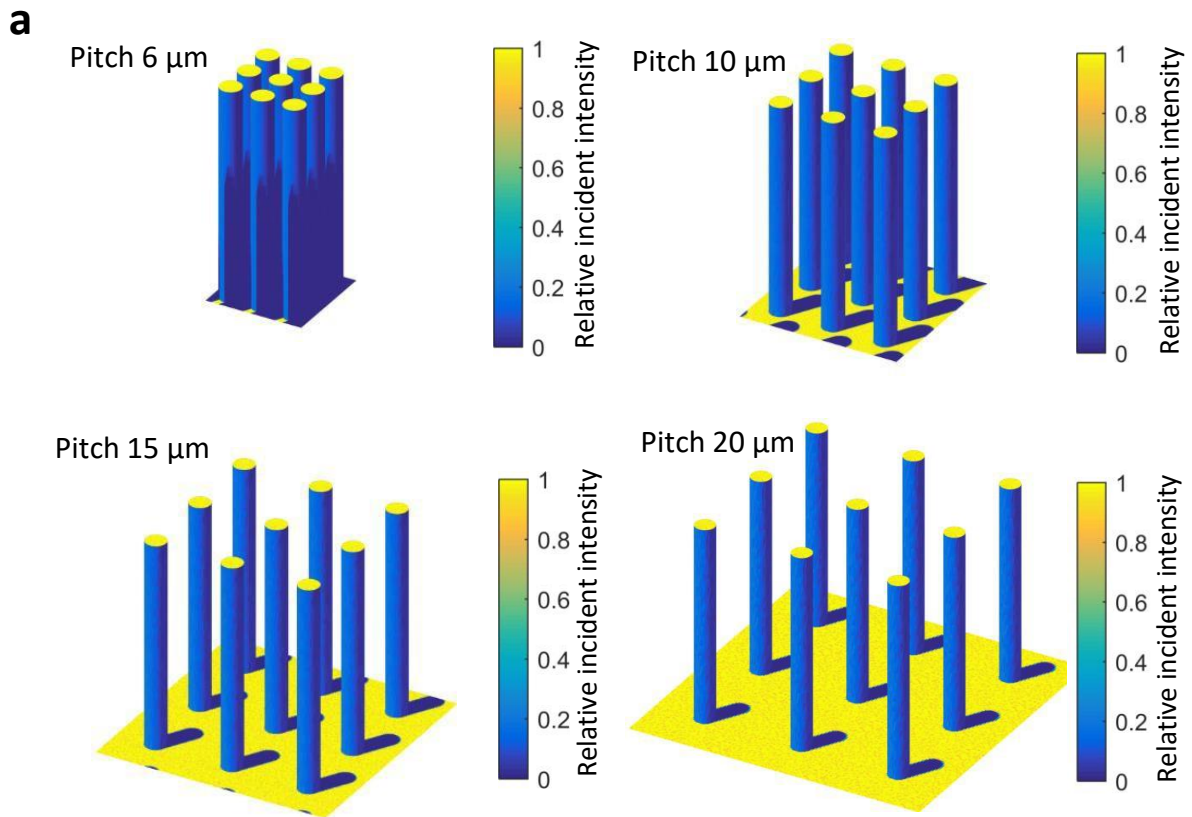**Figure 5.** Sketch of the WO_3/Si micropillar under illumination.

Figure 6. (a) Optical simulations of the intensity distribution map of light illuminated on "metallic" micropillar arrays with different pillar pitch, 6 μm, 10 μm, 15 μm, and 20 μm. (Pillar height 40 μm; light incident angle 1°). (b) Optical simulation results of the total surface area with area of light intensity >0.2 under different incident angle (red curve), and the total surface area (blue curve) for micropillar arrays with different pillar pitch.
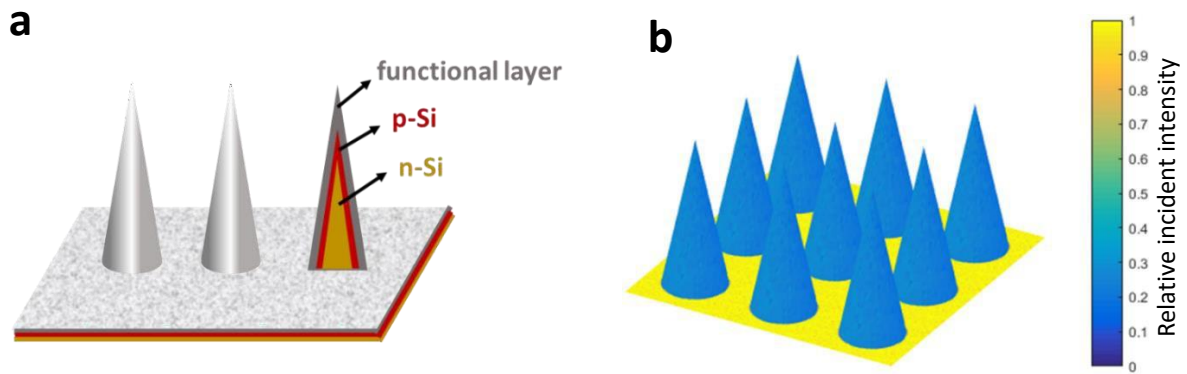
Figure 7. (a) A promising cone-shape micro structure with p-n junction. (b) Optical simulation of the light intensity map of the cone-shape micro structure under illumination (light incident angle 1°).
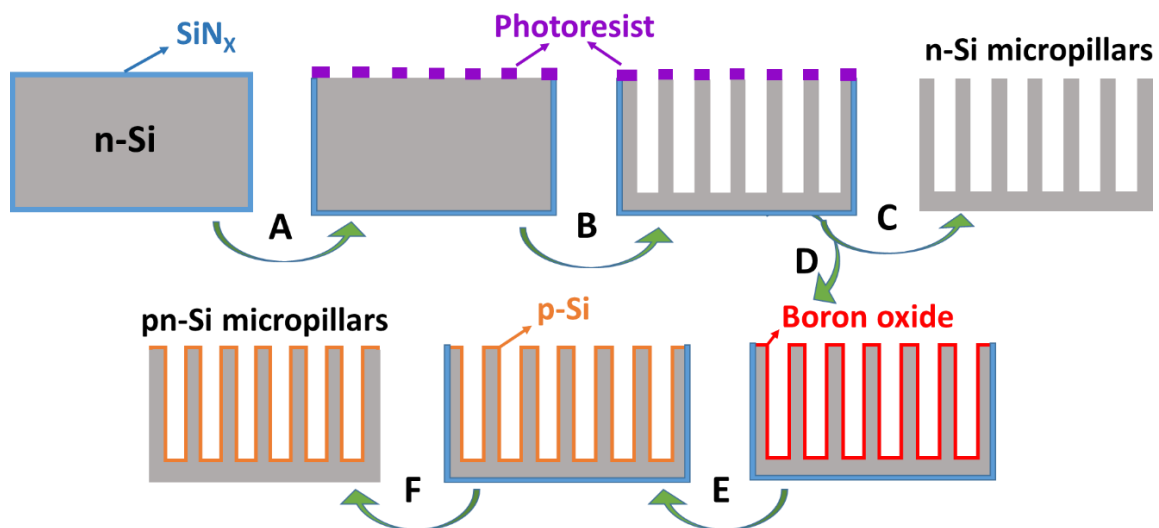

Figure 8. Schematic fabrication process of n-Si and pn-Si micropillar arrays. (A) Removal of topside silicon nitride (SiNx) followed by photolithography. (B) Deep reactive ion etching of Si. (C) Removal of photoresist and SiNx. (D) Boron oxide deposited from solid source. (E) Formation of the radial junction, by a drive-in step at 1050 °C for 15 min. (F) Removal of SiNx.

Well-defined WO_3/n-Si and WO_3/pn-Si micropillar arrays are fabricated and subjected to a quantitative analysis of the relation between the geometry and PEC activity. It is found that a reduced pillar pitch results in areas of low light intensity due to shadowing effect and increases the dead layer of the p-n junction Si surface, which results in a decreased PEC activity.

Photoelectrochemistry

Yihui Zhao, Pieter Westerik, Rudi Santbergen, Erwin Zoethout, Han Gardeniers, Anja Bieberle-Hütter*

From Geometry to Activity: A Quantitative Analysis of WO₃/Si Micropillar Arrays for Photoelectrochemical Water Splitting
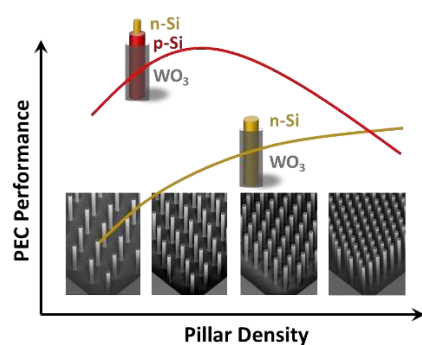
Supporting Information

From Geometry to Activity: A Quantitative Analysis of WO₃/Si Micropillar Arrays for Photoelectrochemical Water Splitting

*Yihui Zhao, Pieter Westerik, Rudi Santbergen, Erwin Zoethout, Han Gardeniers, Anja Bieberle-Hütter**

Cystaline Structure of WO₃

The crystalline phase of the WO_3 film was characterized by a Bruker D8 Eco X-ray diffractometer (XRD) with a Cu Kα ($\lambda = 1.5406$ Å) source and a Lynx-eye detector in a grazing incidence configuration at an incident angle of 3° and in the 2θ range from 20° to 60°. Figure S1 shows the GIXRD spectra of the WO_3/Si micropillar arrays elcectrode before (red) and after (black) annealing in Ar at 450°C for 1 h. The diffraction peaks of the pattern after annealing agree well with monoclinic WO_3 corresponding to JCPDS No. 83-0950 indicating that monoclinic WO_3 was obtained after annealing.
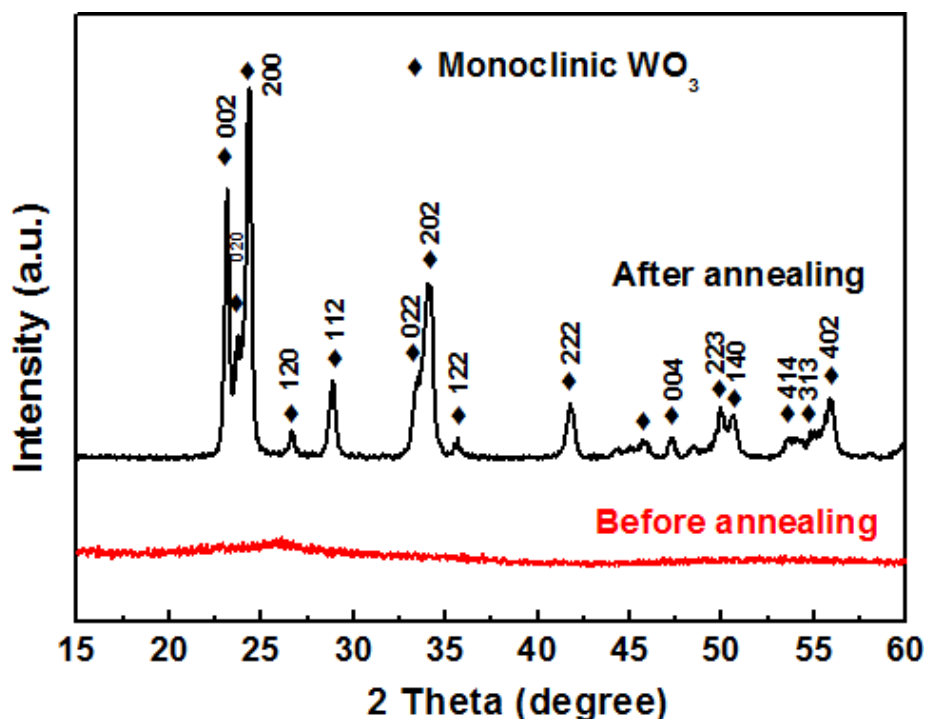

Figure S1: *GIXRD spectra of Si micropilar arrays coated WO₃ after annealing in Ar.*

Light Reflectance

The light reflectance of WO$_3$/Si micropillar array electrodes was investigated using a Perkin Elmer 1050 UV/Vis/NIR spectrophotometer along with 150 mm integrating sphere in the wavelength range of 300 nm to 850 nm with a step size of 5 nm. Figure S2 shows the reflectance spectra of the WO$_3$/Si micropillar arrays with different height and pitch of the pillars. All reflectance curves show a meandering shape as a function of wavelength, which is related to the interference of the light reflected from the WO$_3$ surface and the WO$_3$/Si interface. As shown in Figure S2a, the micropillar array structures have lower light reflectance than the planar electrode. As the pillars become longer, the light reflectance decreases. In the wavelength range below 400 nm (inset in Figure S2a), in which the light is absorbed by the WO$_3$, the reflectance of micropillar array electrodes, with 10 μm height and 40 μm height, decreased around 10% and 15%, respectively, compared with the planar electrode. For 40 μm long pillars, the light reflectance slightly decrease with reduced pillars pitch (Figure S2b).
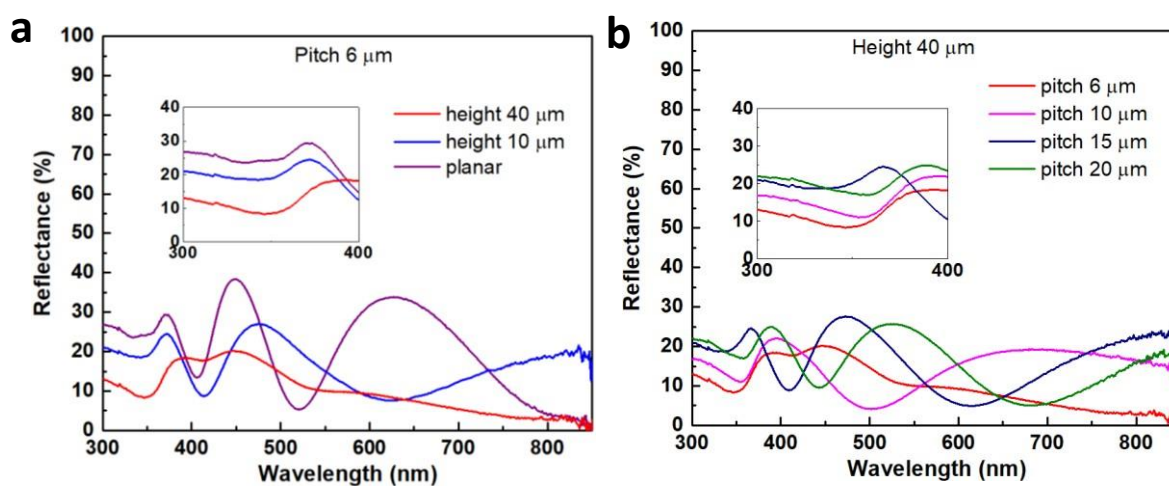

Figure S2: *Reflectance spectra of WO$_3$/Si micropillar arrays with (a) different pillars height, and (b) different pillars pitch.*